Curvilinear 3-D Imaging Using Row--Column-Addressed 2-D Arrays with a Diverging Lens: Feasibility Study

Bouzari, Hamed; Engholm, Mathias; Beers, Christopher; Stuart, Matthias Bo; Nikolov, Svetoslav Ivanov; Thomsen, Erik Vilain; Jensen, Jørgen Arendt

Published in:
IEEE Transactions on Ultrasonics, Ferroelectrics and Frequency Control

Link to article, DOI:
10.1109/TUFFC.2017.2687521

Publication date:
2017

Document Version
Peer reviewed version

Curvilinear 3-D Imaging Using Row–Column Addressed 2-D Arrays with a Diverging Lens: Feasibility Study

Hamed Bouzari, *Member, IEEE,* Mathias Engholm, Christopher Beers, Matthias Bo Stuart, *Member, IEEE,* Svetoslav Ivanov Nikolov, *Senior Member, IEEE,* Erik Vilain Thomsen, and Jørgen Arendt Jensen, *Fellow, IEEE*

***Abstract*—Constructing a double-curved row–column-addressed (RCA) 2-D array or applying a diverging lens over the flat RCA 2-D array can extend the imaging field-of-view (FOV) to a curvilinear volume without increasing the aperture size, which is necessary for applications such as abdominal and cardiac imaging. Extended FOV and low channel count of double-curved RCA 2-D arrays make 3-D imaging possible with equipment in the price range of conventional 2-D imaging. This study proposes a delay-and-sum beamformation scheme specific to double-curved RCA 2-D arrays and validates its focusing ability based on simulations. A synthetic aperture imaging sequence with single element transmissions is designed for imaging down to 14 cm at a volume rate of 88 Hz. Using a diverging lens with f-number of -1 circumscribing the underlying RCA array, the imaging quality of a double-curved $\lambda/2$-pitch 3 MHz 62+62 RCA 2-D array is investigated as a function of depth within a curvilinear FOV of 60°×60°. The simulated double-curved 2-D array exhibits the same full-width-at-half-maximum values for a point scatterer within its curvilinear FOV at a fixed radial distance compared with a flat 2-D array within its rectilinear FOV. The results of this study demonstrate that the proposed beamforming approach is accurate for achieving correct time-of-flight calculations, and hence avoids geometrical distortions.**

I. Introduction

An $N \times N$ element 2-D array can be operated utilizing only $2N$ connections, when a row–column or cross-electrode addressing scheme is used [1]–[7]. This is contrary to the N^2 connections needed, when conventionally addressing the elements. In general, a row–column-addressed (RCA) array is a 2-D matrix array, which is addressed via its row- and column indices. Effectively, it consists of two 1-D arrays arranged orthogonal to each other as shown in Fig. 1. As an example, for a 256+256 RCA array, a 2-D matrix array of equivalent size would have 65,536 elements, over a factor of 7 more than the current state-of-the-art X6-1 PureWave xMATRIX probe from Phillips (Eindhoven, Netherlands) having 9,212 elements [8]. This exhibits the potential of having very large RCA 2-D arrays with low channel count and real-time capabilities.

H. Bouzari*, M. B. Stuart, and J. A. Jensen are with the Center for Fast Ultrasound Imaging, Department of Electrical Engineering, Technical University of Denmark, Kgs. Lyngby, Denmark.

M. Engholm, and E. V. Thomsen are with the Department of Micro- and Nanotechnology, Technical University of Denmark, Kgs. Lyngby, Denmark.

C. Beers is with Sound Technology Inc, Analogic Ultrasound Group, PA-16803, USA.

S. I. Nikolov is with the BK Ultrasound ApS, Herlev, Denmark.

*e-mail of corresponding author is: bouzari@elektro.dtu.dk

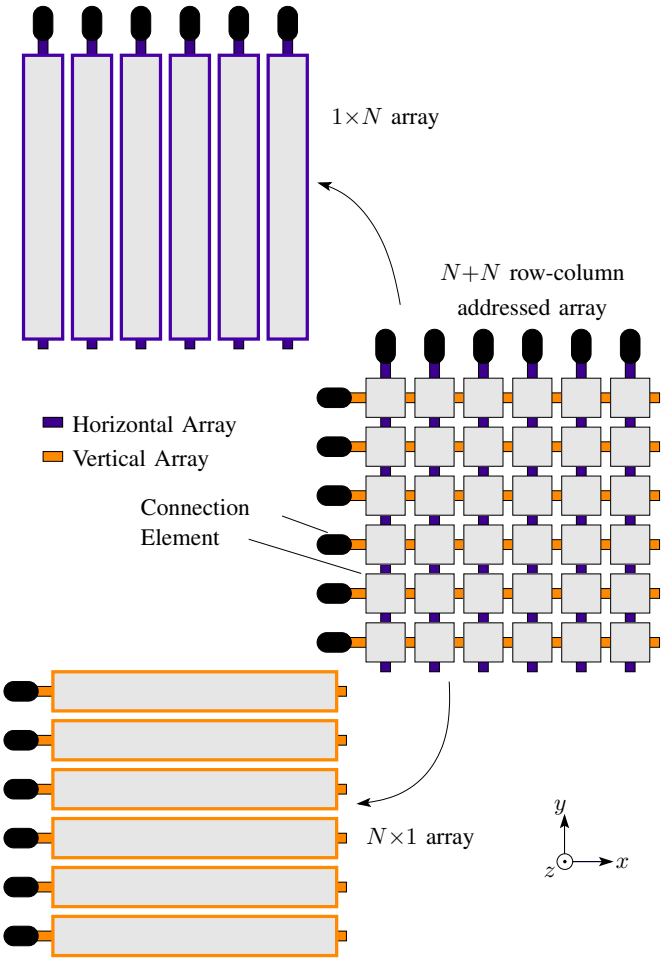

Figure 1. An RCA 2-D transducer array can be interpreted as two orthogonal 1-D arrays. To the right is shown a 2-D transducer array, where each transducer element is addressed by its row or column index, effectively creating the two arrays shown to the left. (drawing from [5])

It has been demonstrated in several studies that row–column technology is a realistic alternative to the state-of-the-art matrix probes, especially as a low-cost alternative [1]–[7], [9]. However, one major issue with the RCA arrays is that they can only emit acoustic energy directly below the array and in a cross-shape to the sides. Therefore, imaging can only be done in a rectilinear region in front of the array. For applications such as cardiac imaging, it is relevant to have a probe with a small foot-print capable of phased array

imaging, such that the heart can be visualized through the ribs. True volumetric phased array imaging is possible with RCA arrays, provided that the array is double curved to spread the energy during transmit [2]. However, manufacturing curved transducer elements is challenging for both capacitive micromachined ultrasonic transducer (CMUT) and piezoelectric transducer (PZT) technologies. Another approach to spread the acoustic energy is by using a double curved diverging acoustic lens on top of the RCA array [10]. Using a lens makes it easier to fabricate curved arrays, as it is not needed to manufacture curved elements, and also making a lens is a well-tested technology. An in-depth study of the possibilities in this approach is therefore the main goal of this study.

Initial results of this study have been published as a conference proceeding [11]. In this paper, a more detailed discussion on the pros and cons of using a diverging lens is presented. The curvilinear volumetric imaging performance of an RCA array equipped with a diverging lens is investigated based on Field II [12], [13] simulations. The quality assessments of the B-mode images, *i.e.*, spatial resolution and contrast resolution, are carried out based on the simulations using synthetic aperture imaging (SAI) technique. The SAI sequence is designed for imaging down to 14 cm of depth.

The paper is organized as follows: The current limitations with flat RCA arrays are discussed in Section II-A, and different approaches to disperse the acoustic energy are introduced in Section II-B. Section II-C presents an overview of the delay-and-sum (DAS) beamformation with a double curved RCA, and the utilized SAI sequence is explained in Section III-A. In Section III-B, the imaging quality assessment measures are explained. In Section III-C, a detailed overview of the simulation setup is presented. Section IV explains and discusses the simulation results with an RCA 2-D array equipped with a diverging lens. The final section concludes the paper with suggestions for future work.

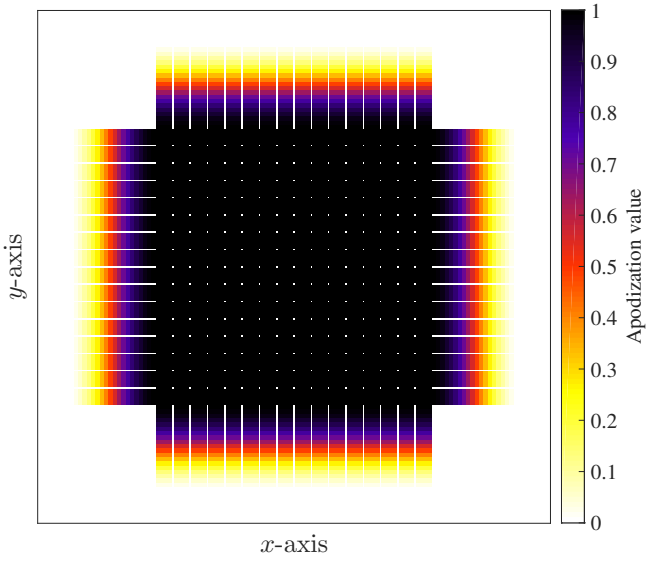

Figure 2. The static roll-off apodization layout is applied to either ends of the line-elements of the array, *e.g.*, here a 16+16 RCA array with roll-off apodization regions is shown. The central region, shown in black, has an apodization value of one. Each roll-off region is connected to each line-element.

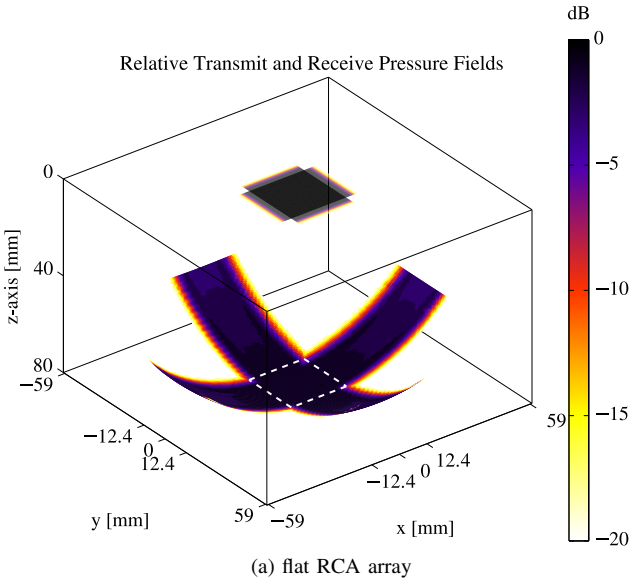

(a) flat RCA array

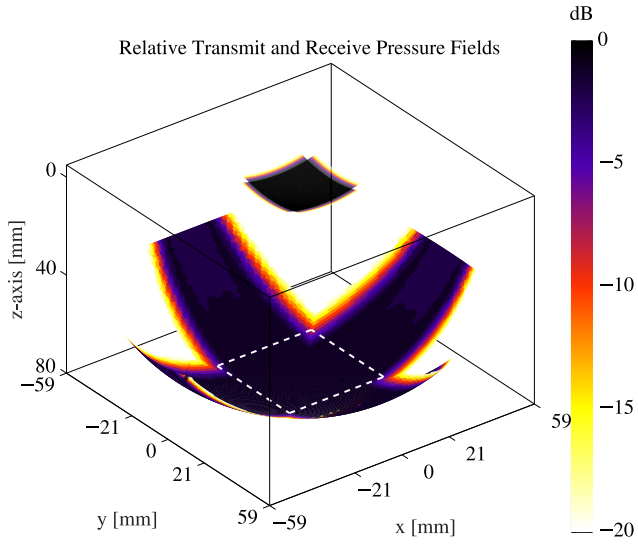

(b) curved RCA array

Figure 3. Relative transmit and receive pressure fields at radial distance of 80 mm for azimuth and elevation steering angles from –45° to 45°. The imaging area is the intersection of these two fields, which is (a) the rectilinear forward-looking box, and (b) the curvilinear forward-looking region in front of the transducer using a lens with $f_{\#} = -1$.

II. RCA 2-D Arrays

A. Flat RCA 2-D Arrays

In 3-D ultrasound imaging with flat RCA 2-D arrays, the two orthogonal 1-D transmit and receive arrays are both used for focusing in the lateral and elevation directions separately. Each of the two 1-D arrays can electronically focus in one lateral dimension, when delays are applied to the elements in the array. One of the 1-D arrays is used to transmit ultrasound into the object of interest. For example, the transmit array is able to focus the beam in the x- and z-directions, whilst no electronic transmit focusing can be performed in the y-direction. As a result, the emitted ultrasound is focused along a line parallel to the y-direction. By adjusting the delays on the transmit elements, this focal line may be translated to any position

in the xz-plane. The orthogonal 1-D array then receives the echoes scattered from the illuminated region of the volume. By applying delays, the received signals can also be focused in a line normal to any position in the yz-plane. The combination of the two orthogonal line-foci of the transmit and receive array produces a point focus in the volume. By translating this focus throughout the volume, a 3-D rectilinear image may be formed.

DAS beamformers usually assume the geometry of the sound sources and receivers to be points. However, by row–column addressing the elements on a 2-D matrix array, each row and column is acoustically equivalent to a line-element. Furthermore, the emitted wavefront of a line-element has the shape of a cylinder, *i.e.*, it is a plane wave in the plane aligned along the line-element and a circle arc in the plane orthogonal to the line-element. Assuming the geometry of the line-elements to be points is therefore a poor approximation. A more accurate approximation assumes the line-elements to be line segments instead of points, and the beamformer should calculate the distances between line-elements and the point [5]. However, the long length of the line-elements results in prominent edge effects [2], [5]. These edge effects are due to the limited size of the aperture and originates from both ends of the line-element. It was shown that using a static roll-off apodization as shown in Fig. 2 along each row and column element reduces those edge effects without altering the main echo response [5], [9].

Due to the perpendicular orientation of the transmit and receive fields as shown in Fig. 3a, the pulse-echo field for the flat RCA 2-D array is limited to the forward looking rectilinear region in front of the transducer. The strips in Fig. 3a show the transmit and perpendicular receive pressure fields at the depth of 80 mm, when steering the beam to the sides. The transmit-receive pressure field, however, is then the multiplication of those fields or their summation in decibel scale. Both transmit and receive beams were steered by $\pm 45°$. When the horizontal array is used as a transmit array, it can steer the transmit beam in the z-x plane, and at the same time the vertical array is receiving in the z-y plane. Therefore, the transmit-receive pressure field at the sides is about 20 dB lower in amplitude than the rectilinear forward looking region inside the dashed rectangle. Although the transmit beam is insonifing those regions, the receive beam has a 20 dB lower amplitude at those side regions. At the corner regions, the transmit-receive pressure field is about 40 dB lower than the rectilinear forward looking region. This is because both the transmit and receive pressure beams have 20 dB lower amplitudes at those corner regions. Therefore, to be able to visualize those regions, a 40 dB larger dynamic range is needed or a gain compensation for those regions is required. However, the region indicated by white dashed lines, which is the intersection of transmit and receive pressure fields, can be imaged at any depth uniformly.

B. Curved RCA 2-D Arrays

Using a double-curved RCA 2-D array can extend the volumetric imaging field-of-view (FOV) to a curvilinear region. To spread the acoustic energy of a line-element curvilinearly along its larger dimension, it has to be curved to generate a diverging wave. The defocusing of the waves can be made by using a fixed electronic delay profile along each flat line-element, similar to a fixed first stage in micro-beamforming with 2-D arrays [14]. Another approach is to use a double curved diverging acoustic lens on top of the flat RCA array [10].

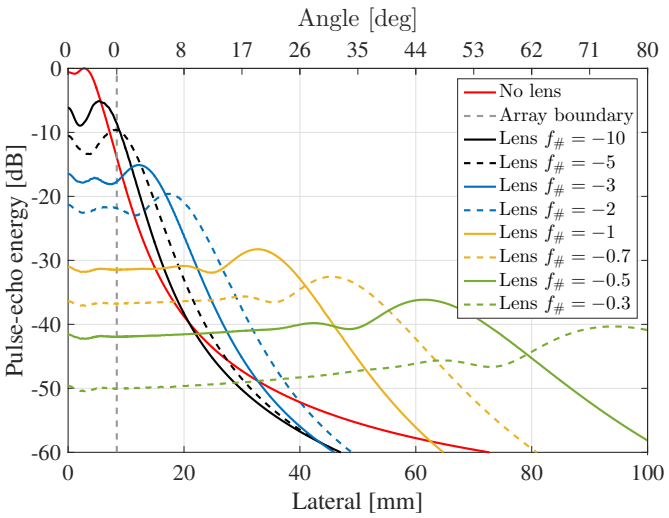

Figure 4. Reduction in the pulse-echo energy using a diverging lens relative to a flat transducer. The points are located on a line at 80 mm away from the surface of the transducer.

A concave diverging lens could be designed with a material, which has lower speed of sound compared to the human tissue. It will have a higher thickness around the corners and the sides of the array, and less thickness close to center of the array. Alternatively, a convex diverging lens can be made from a material with a higher speed of sound compared to the human tissue, which is preferred for a better contact surface. A flat diverging lens also can be made by using a combination of two different materials, one with higher and other one with lower speed of sound compared to the human tissue.

In Fig. 4 the pulse-echo energy as a function of lateral position for different lens f-numbers ($f_\#$) is illustrated on an RCA array. The $f_\#$ is defined as a ratio between the focal distance to the lens diameter. The pulse-echo energy drops by moving away from the forward looking region of the array. At approximately 8° steering angle the pulse-echo energy drops by 40 dB, when no lens is used. However, by using a diverging acoustic lens on top of an RCA 2-D array, a larger FOV can be illuminated. The FOV can be adjusted by using different $f_\#$ values for the lens. By using a diverging lens with $f_\# = -1$, the overlapped transmit and receive region increases to about $\pm 30°$ in both directions as shown in Fig. 3b compared to Fig. 3a.

Note that, for the same aperture size, lower $f_\#$ values for the lens corresponds to larger thicknesses of the lens and therefore the attenuation becomes higher through the lens material. Thus, there is a trade-off between FOV and attenuation. For example the delay profile can be in a range of 0 µs to 3.5 µs for a lens with $f_\# = -0.7$ and a speed of sound of 1400 m/s, which corresponds to a thickness range of 0 mm to 5 mm. A suitable material for a lens could be Sylgard 160 (PDMS) with a density of 1580 kg/m^3 and a speed of sound of 950 m/s and attenuation

of $0.4f^{1.4}$ dB/(cm MHz), where f is the operating frequency in MHz. Therefore, for an operating frequency of 3 MHz the maximum attenuation is 6.14 dB at the largest thickness [15]. This might be compensated by doubling the amplitude of the excitation pulse.

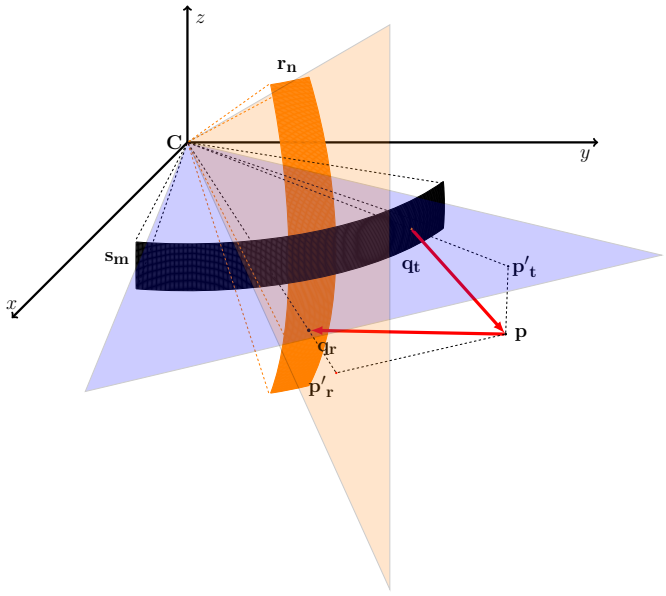

Figure 5. The time-of-flight of a wavefront is given by the shortest distance from the source $\mathbf{s}_m$ to the point being focused $\mathbf{p}$ and back to the receiving element $\mathbf{r}_n$, divided by the speed of sound.

C. DAS Beamforming with Curved RCA 2-D Arrays

The time-of-flight (ToF) of a wavefront is given by the shortest distance from the arc source $\mathbf{s}_m$ to the point being focused $\mathbf{p}$, and back to the receiving element $\mathbf{r}_n$, divided by the speed of sound. Using the notations from Fig. 5 this can be written as:

$$\mathrm{ToF}_m(n,\mathbf{p}) = \frac{d(\mathbf{s}_m,\mathbf{p}) + d(\mathbf{r}_n,\mathbf{p})}{c}, \tag{1}$$

where c is the speed of sound in the medium, n is an index from 1 to the number of receive line elements N, and m is the emission index. The function $d(.,.)$ calculates the shortest distance between an arc and a point in space, which will be defined in the remainder of this section.

The arc segment from point $\mathbf{a}$ to point $\mathbf{b}$ with center $\mathbf{c}$ is termed $\overset{\frown}{\mathbf{ab}}$ assuming the center at the origin. This is illustrated in Fig. 6. The projection of point $\mathbf{p}$ onto the plane passing through the arc $\overset{\frown}{\mathbf{ab}}$ is termed $\mathbf{p}'$ and is determined by the usual equation for projection. To determine if the vector $\mathbf{cp}'$ is in between vector $\mathbf{ca}$ and vector $\mathbf{cb}$, we define the normalized cross products $\hat{l}_a$ and $\hat{l}_b$ as

$$\hat{l}_a = \frac{\mathbf{cp}' \times \mathbf{ca}}{\|\mathbf{cp}'\|\|\mathbf{ca}\|}, \tag{2}$$

$$\hat{l}_a = \frac{\mathbf{cp}' \times \mathbf{cb}}{\|\mathbf{cp}'\|\|\mathbf{cb}\|}. \tag{3}$$

Depending on the location of the point $\mathbf{p}$, vectors $\hat{l}_a$ and $\hat{l}_b$ can be either $\hat{j}$ or $-\hat{j}$, where $\hat{j}$ is the unit vector of the z-axis. $\hat{l}_a$ and $\hat{l}_b$ have different signs, when $\alpha_1 \leq \phi \leq \alpha_2$ and same sign, when $\alpha_2 \leq \phi$ or $\phi \leq \alpha_1$, where α_1, α_2, and ϕ are the angles between the x-axis and vectors $\mathbf{ca}$, $\mathbf{cb}$, and $\mathbf{cp}$, respectively, as shown in Fig. 6.

When $\hat{l}_a$ and $\hat{l}_b$ have different signs, *i.e.* $\hat{l}_a = \hat{j}$ and $\hat{l}_b = -\hat{j}$, or $\hat{l}_a = -\hat{j}$ and $\hat{l}_b = \hat{j}$, the standard formula for the distance between an arc and a point can be used:

$$d = \sqrt{\|\mathbf{pp}'\|^2 + \left(\|\mathbf{cp}'\| - R\right)^2}, \tag{4}$$

where R is the curvature of the arc and equals to $\|\mathbf{ca}\|$ or $\|\mathbf{cb}\|$.

When $\hat{l}_a$ and $\hat{l}_b$ have the same signs, *i.e.* $\hat{l}_a = \hat{j}$ and $\hat{l}_b = \hat{j}$, or $\hat{l}_a = -\hat{j}$ and $\hat{l}_b = -\hat{j}$, the shortest distance from the arc segment to the point is the distance from the closest end of the arc segment ($\mathbf{a}$ or $\mathbf{b}$) to the point $\mathbf{p}$. The following therefore determines the minimum distance between the point $\mathbf{p}$ and the arc segment $\overset{\frown}{\mathbf{ab}}$:

$$d(\overset{\frown}{\mathbf{ab}},\mathbf{p}) = \begin{cases} \sqrt{\|\mathbf{pp}'\|^2 + \left(\left\|\|\mathbf{cp}'\| - R\right\|\right)^2} & \text{if } \left| \begin{array}{l} \hat{l}_b = -\hat{j} \text{ and } \hat{l}_a = \hat{j} \\ \hat{l}_b = \hat{j} \text{ and } \hat{l}_a = -\hat{j} \end{array} \right. \\ \|\mathbf{ap}\| & \text{if } \hat{l}_b = -\hat{j} \text{ and } \hat{l}_a = -\hat{j} \\ \|\mathbf{bp}\| & \text{if } \hat{l}_b = \hat{j} \text{ and } \hat{l}_b = \hat{j}\ . \end{cases} \tag{5}$$

Using (5), the distances $d(\overset{\frown}{\mathbf{s}_m},\mathbf{p})$ and $d(\overset{\frown}{\mathbf{r}_n},\mathbf{p})$ can now be determined. The focused signal at point $\mathbf{p}$ is calculated by summing all receive signals at the time instances given by (1):

$$z_m(\mathbf{p}) = \sum_{n=1}^{N} a_{\mathrm{elec}}(n,\mathbf{p}) y_{m,n}(\mathrm{ToF}_m(n,\mathbf{p})), \tag{6}$$

where N is the number of receive elements, a_{elec} is the electronic receive apodization, and $y_{m,n}(t)$ is the measured signal from emission m on the receive element n at time t.

The synthetic transmit aperture (STA) focused signal at point $\mathbf{p}$ is calculated by summing the focused signals from all emissions:

$$l_{STA}(\mathbf{p}) = \sum_{m=1}^{M} b_{\mathrm{elec}}(m,\mathbf{p}) z_m(\mathbf{p}), \tag{7}$$

where M is the number of transmissions, b_{elec} is the electronic transmit apodization, and $z_m(\mathbf{p})$ is the focused received signal from emission m at point $\mathbf{p}$. In general, both a_{elec} and b_{elec} are dependent on the imaging point $\mathbf{p}$ so that, a dynamic apodization can be achieved in transmit and receive. In this study however, they are fixed to an apodization window, *e.g.*, Hanning, for all imaging points.

III. Methods

A. Synthetic Aperture Imaging Technique

In conventional ultrasound imaging it will be a tedious method to transmit for each steering angle so many times to

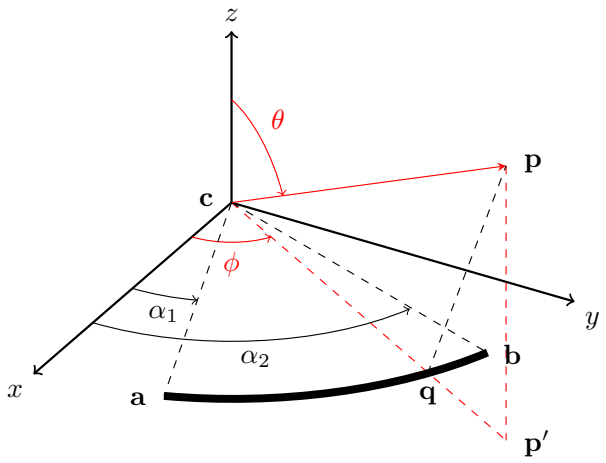

Figure 6. Distance between a point $\mathbf{p}$ and an arc $\overset{\frown}{\mathbf{ab}}$ is calculated using (5).

cover the whole volume. However, this will not be a problem, if a SAI technique is used [16]. Thereby, all the transmit delay calculations can be done after the acquisition. A SAI sequence is designed for imaging down to 14 cm of depth. It utilizes single element transmissions on the row elements and the echoes are collected with all the column elements. For a speed of sound of 1540 m/s, 182 µs is required to acquire a single image line to a depth of 14 cm. For 62 emissions this is equivalent to a volume rate of 88 Hz. IQ-modulated RF data are used for beamforming a low-resolution volume for every emission and finally, by summing all the low-resolution volumes, a high-resolution volume is generated.

B. Imaging Quality Assessment Measures

The imaging performances of a double-curved RCA 2-D array is computed using the two measures described below:

1) Spatial Resolution: The spatial resolution is calculated as the full-width at half-maximum (FWHM) of the imaging system's point spread function (PSF).

2) Contrast resolution: The contrast resolution is calculated as the cystic resolution (CR), which is the ability to detect an anechoic cyst in a uniform scattering medium [17]–[19]. The relative intensity (RI) of a PSF is quantized as the clutter energy to total energy ratio,

$$\mathrm{RI}(R) = \sqrt{\frac{E_{out}(R)}{E_{tot}}} = \sqrt{1 - \frac{E_{in}(R)}{E_{tot}}}, \qquad (8)$$

where E_{in} is the signal energy inside a circular region with radius, R, centered at the peak of the point spread function, E_{tot} is the total PSF energy, and E_{out} is the PSF energy outside the circular region. The $\mathrm{RI}(R)$ curve can be compressed to a single number by sampling the curve at *e.g.* 20 dB. The result is the required cyst radius at which the intensity at the cyst's center is 20 dB lower than its surroundings, written as $R_{20\mathrm{dB}}$.

C. Simulation Setup

In this study, Field II [12], [13] is used for all simulations. A MATLAB (MathWorks Inc., Massachusetts, USA) beamformer

Table I
TRANSDUCER AND SIMULATION PARAMETERS.

Parameter name	Notation	Value	Unit
Number of elements	–	62+62	–
Center frequency	f_0	3.0	MHz
Speed of sound	c	1480	m/s
Wave length	λ	493.3	µm
Array pitch -x	d_x	$\lambda/2 = 246.6$	µm
Array pitch -y	d_y	$\lambda/2 = 246.6$	µm
Sampling frequency	f_s	120	MHz
Emission pulse	–	2-cycles, Hann-weighted	–
Lens focal ratio	$f_\#$	-1	–

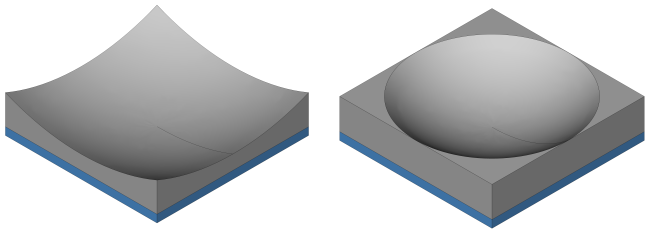

(a) lens circumscribes the array (b) lens inscribes the array

Figure 7. Lens (a): circumscribes the array and (b): inscribes in the array. In case (a) the effective FOV is less than the f-number of the lens. In case (b) the FOV is equal to that of the lens. The lens material is shown in gray and the array is shown in blue.

that implements (7) was programmed to beamform data from curved RCA arrays and produce the PSFs included in this paper. The simulation parameters of a RCA 62+62 element 2-D array are shown in Table I. The receive array is rotated 90° with respect to the transmit array. Field II is set up to use lines to describe the apertures and each line-element is divided into square mathematical sub-elements with a side length of $\lambda/4$. To remove the otherwise apparent secondary echoes originating from the either ends of line-elements, two roll-off apodization regions are placed at both ends of each element [5], [9]. The length of each apodization region was equal to 15 times the pitch of the array. Each mathematical sub-element in both transmit and receive arrays is delayed according to the lens delay profile and no attenuation is assumed for

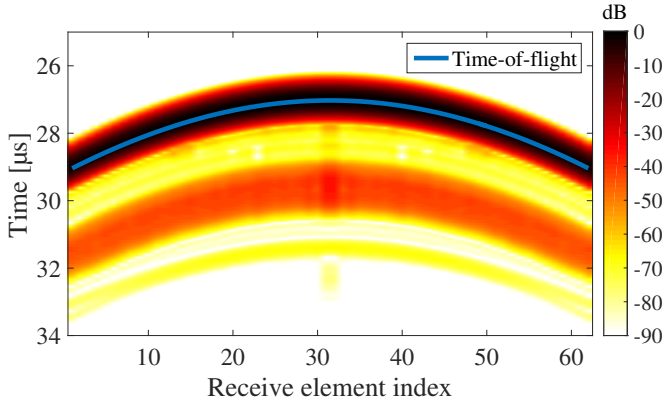

Figure 8. The image is the envelope of the received signals from a single element emission reflected by a scatterer located at (x, y, z) = (0,0,20) mm and the overlaid blue line is the predicted time-of-flight calculated using (6).

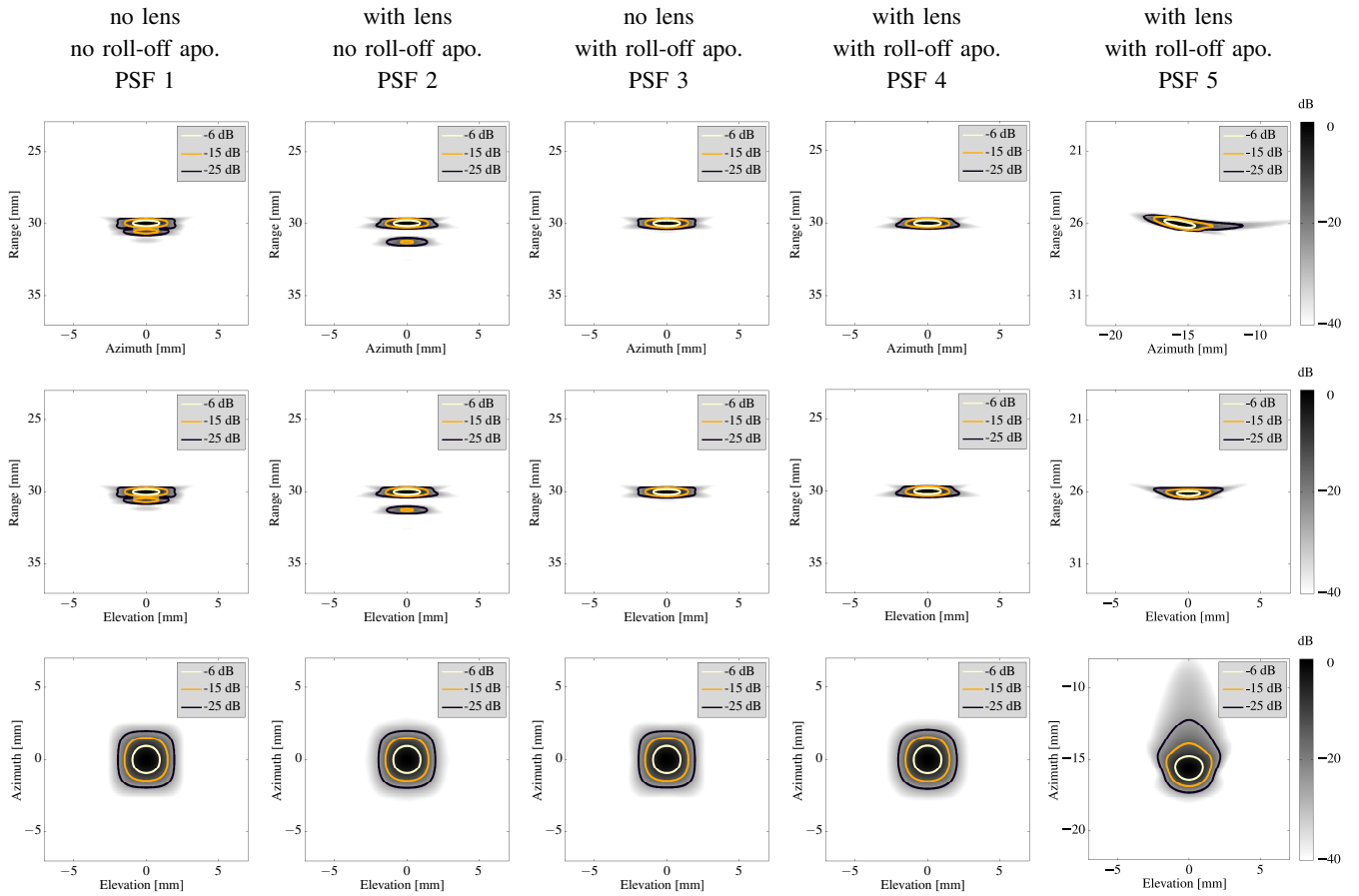

Figure 9. Three cross-planes (azimuth, elevation, and C-plane) of 3-D PSFs are shown at a dynamic range of 40 dB. The origin corresponds to the center of the transducer surface aligned with a point target positioned at (x, y, z) = (0, 0, 30) mm for PSF 1 $\sim$ PSF 4, and a point target positioned at (x, y, z) = (0, -15, 25.9) mm for PSF 5. The C-planes are at depth of 30 mm for PSF 1 $\sim$ PSF 4 and at depth of 25.9 mm for PSF 5.

the lens. Theoretically, transmitting with row elements and receiving with column elements should image exactly the same curvilinear volume as transmitting with column elements and receiving with row elements. Thus, no preference is considered in transmitting with row elements and receiving the echoes with column elements, or vice versa.

The equation (1) is introduced for beamforming with a general double-curved convex RCA 2-D array. By using only single material for the lens, the lens delay profile matches the lens concave surface curvature. In this case, the concave lens can be estimated with a double-curved convex array for which the equation (1) applies. It is assumed that the lens has no thickness at the center. If the lens thickness is different than zero at the center, a constant delay term accounting for that thickness has to be added to (1). However, if the lens part is made out of two materials with different speeds of sound, the curvature of the produced wavefront can be different to the lens surface curvature. In this case, a lens part with a flat or convex surface can be made.

Fig. 7 illustrates two different ways to integrate a diverging lens over the array. The lens shown in Fig. 7a circumscribes the whole underlying array. On the other hand, the lens shown in Fig. 7b does not cover the whole array, instead the lens is inscribed in the array. In this configuration, essentially there is no diverging focusing applied to the end-most elements, and all elements between the end and the middle have compromised divergence. Thus, the defocusing is applied inconsistently across the array.

Both inscribed and circumscribed cases can provide apodization from lens attenuation as the lens becomes thicker toward the edges. The circumscribed case actually provides more apodization because in this case the lens gets thicker in the corners than the inscribed lens. The inscribed lens is advantageous because it has a smaller lens arc height and shorter chord length than the circumscribed lens. This reduced arc height improves patient contact possibilities, but, more importantly, the shorter chord length enables lower $f_{\#}$ defocusing. Fresnel lens could be another configuration as a diverging lens, however in this study the configuration shown in Fig. 7a has been chosen for the simulations.

IV. Results and Discussion

The beamformer can IQ-beamform 250,000 voxels from a complex data set of 1.5 MiB from 62 receive line elements in approximately 14.1 s on a PC with a 3.4-GHz Intel Core i7-4770 CPU (Intel Corp., Santa Clara, CA, USA) and 32 GiB of RAM. The proof-of-concept Matlab implementation of the beamformer can therefore not achieve a frame rate useful

for real-time applications, but the frame rate is adequate for research purposes.

Fig. 8 shows the received echoes that are generated from a single scatterer located at $(x,\ y,\ z) = (0,\ 0,\ 20)$ mm. The secondary echoes after the main echo are suppressed below –40 dB by using the static roll-off apodization regions. The overlaid blue line is the predicted time-of-flight using (6).

Fig. 9 shows five 3-D PSFs simulated with Field II [12], [13] using SAI technique and beamformed for both flat and curved RCA 2-D array. The point targets are located at $(x,\ y,\ z) = (0,\ 0,\ 30)$ mm and $(x,\ y,\ z) = (0,\ -15,\ 25.9)$ mm and a Hanning electronic apodization is applied over the received RF data. A Hanning apodization is applied over the low-resolution volumes before summing in the SAI technique. The PSFs are normalized to their maximum value and shown in a dynamic range of 40 dB. For the PSF 1 and PSF 2, the roll-off apodization is disabled.The secondary lobes located slightly after 30 mm depth in PSF 1 and PSF 2 are the apparent edge echoes and cannot be suppressed by using the electronic apodization. On the other hand, for the PSF 3 $\sim$ PSF 5, the roll-off apodization is activated. It can be noticed that the apparent secondary echoes after each main echo in both PSF 3 and PSF 4 are suppressed by using the static roll-off apodization regions. Using the roll-off apodization does not change the lateral resolution of the main echo, this can be seen by comparing PSF 1 and PSF 2 with PSF 3 and PSF 4. The effect of roll-off apodization is mostly outside of the curvilinear imaging FOV of the array, and therefore will not affect the lateral resolution within the imaging FOV. Table II lists the FWHM and the CR of the simulated 3-D PSF 3 $\sim$ PSF 5 shown in the Fig. 9.

Table II
FWHM AND CR OF SIMULATED 3-D PSF 3 $\sim$ PSF 5 SHOWN IN FIG. 9

		PSF 3	PSF 4	PSF 5	
CR	$R_{6\text{dB}}$	0.68	0.68	0.97	mm
	$R_{12\text{dB}}$	1.11	1.12	1.55	mm
	$R_{20\text{dB}}$	1.61	1.64	2.8	mm
FWHM	Radial	0.37	0.37	0.38	mm
	Azimuth	1.88	1.9	1.9	mm
	Elevation	1.88	1.9	1.64	mm

Due to beam divergence, the PSF 2 has a 12 dB lower amplitude compared with PSF 1. Similarly, PSF 4 and PSF 5 have lower amplitudes compared with PSF 3 by 11 dB and 7 dB, respectively.

To study the PSF characteristics as a function of lateral angular position and radial distance, a point scatterer is imaged by sweeping it from 0° to 40° in the lateral plane with steps of 10° at radial distances from 10 mm to 60 mm from the center of the array. At each radial distance and angular position the FWHM and CR values are calculated over a volume of 10 mm×10 mm×10 mm surrounding the point target. Fig. 10 is illustrating the measured FWHM and CR values as a function of depth and angular position in lateral plane.

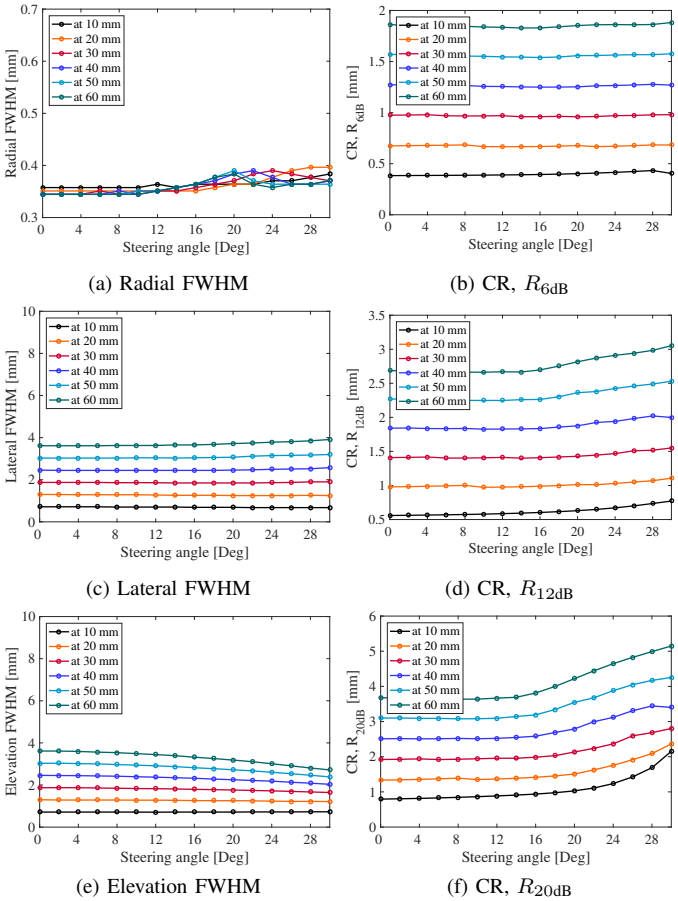

(a) Radial FWHM (b) CR, $R_{6\text{dB}}$

(c) Lateral FWHM (d) CR, $R_{12\text{dB}}$

(e) Elevation FWHM (f) CR, $R_{20\text{dB}}$

Figure 10. CR and FWHM values calculated for point targets located at radial distances from 10 mm to 60 mm as a function of different azimuth steering angle away from the central forward-looking axis of the array.

Using multiple elements in the transmit or receive and by adjusting their delays, the flat RCA 2-D array generates a focal line, however, with a curved RCA 2-D array, focusing in transmit or receive generates two intersection points instead of a focal line as shown in Fig. 11. Similar to flat RCA 2-D array, either of these two intersection points can be focused in receive and in this way suppressing the secondary intersection points in both transmit and receive. Looking at Fig. 11, it can be noticed that the characteristics of the focused intersections can be different at different angles. Moving away from the center of the elements towards the edges, the transmit wavefronts contact each other at a sharper angle compared with the contact point at the center. It can be observed in Fig. 10 that by moving away from the center towards the higher angular position in lateral plane, the elevation FWHM values become smaller while the CR values become larger. On the other hand, the lateral FWHM values stay constant, this is due to the intersection of the wavefronts in the receive direction which is at the center of the receive elements and therefore the elevation FWHM values stay constant for all angular positions in the lateral plane.

Fig. 12 illustrates three cross-planes (azimuth, elevation, and C-plane) of a phantom with point targets in water simulated with and without a diverging lens. The point targets are

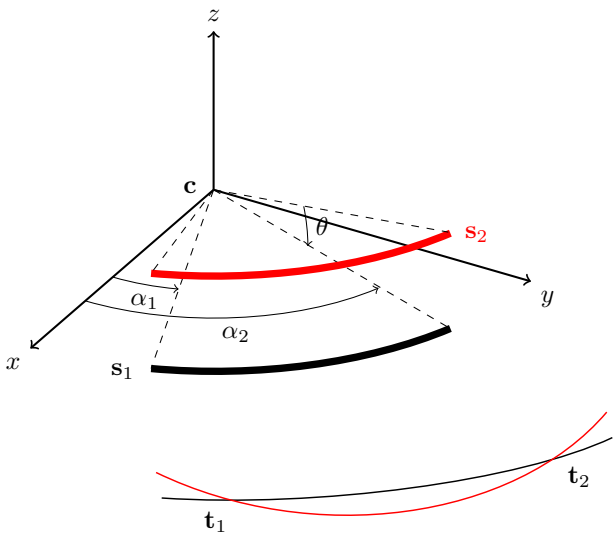

Figure 11. Focusing the wavefronts at a fixed distance with arc-shaped elements $\mathbf{s}_1$ and $\mathbf{s}_2$ generates two intersection points $\mathbf{t}_1$ and $\mathbf{t}_2$. In conventional row-column imaging either of these intersections can be identified in receive.

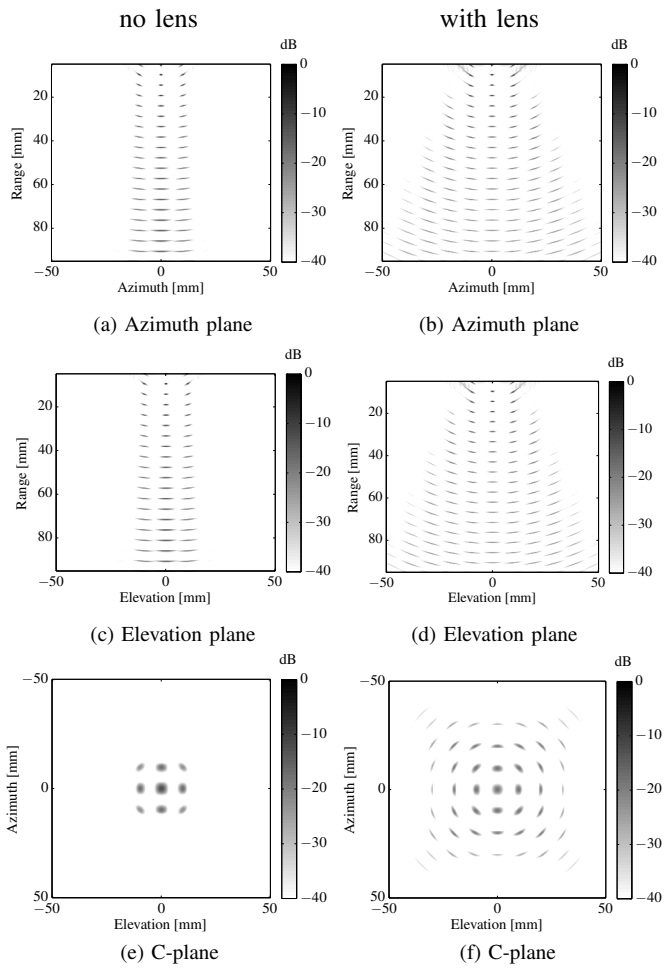

Figure 12. Three cross-planes (azimuth, elevation, and C-plane) of a phantom with point scatterers axial and lateral spacing of 5 mm and 10 mm imaged with and without a diverging lens ($f_{\#} = -1$), are shown at a dynamic range of 40 dB. The C-planes are at depth of 47 mm.

distributed in both lateral and elevation dimensions from –60 mm to 60 mm with step size of 10 mm, as well as in an axial range of 5 mm to 95 mm with step size of 4.5 mm. It can be seen from Fig. 12 that, by using a diverging lens the FOV is extended compared to the flat RCA array. For the case without a lens, the width of the array including the apodization regions is (62+2*15)*λ/2, which corresponds to the 40 dB lateral FOV shown in Fig. 12. For the case with a lens, the 40 dB lateral FOV matches the lens with an $f_{\#} = -1$.

Fig. 13 illustrates three cross-planes (azimuth, elevation, and C-plane) of an anechoic cyst vessel phantom simulated with and without a diverging lens. The phantom with volume size of 40×40×20 mm^3 contains an anechoic cyst vessel with radius of 5 mm along the azimuth dimension located at a 20 mm depth. The phantom is simulated in water with average scatterer density of 8 per mm^3. The FOV is extended compared to the flat RCA array. In Fig. 14, the cyst phantom is located deeper at a 60 mm depth and beamformed with the proposed DAS beamforming method, with and without a diverging lens. Similar to Fig. 13 here also using a diverging lens extends the FOV compared to the flat RCA array.

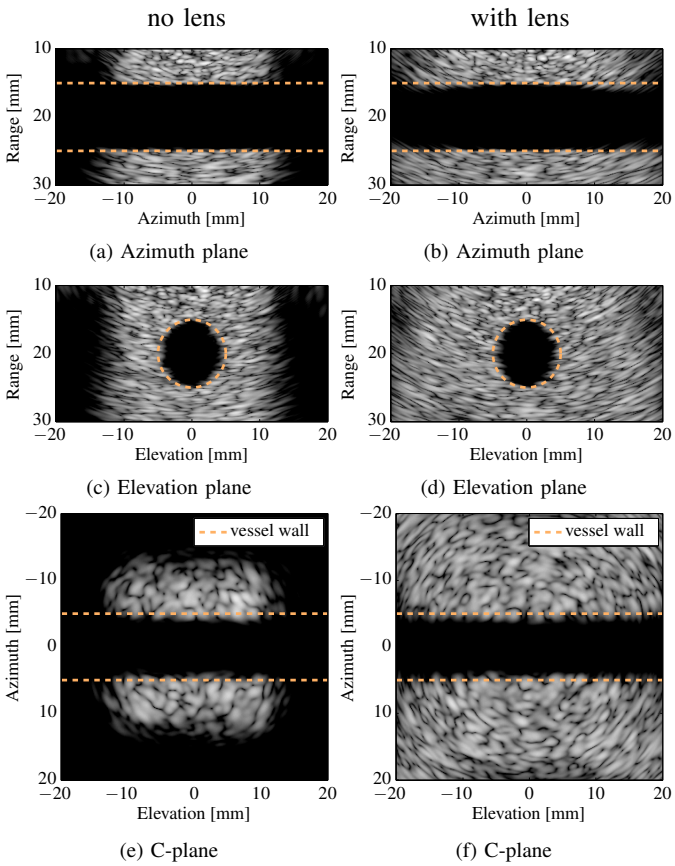

Figure 13. Three cross-planes (azimuth, elevation, and C-plane) of a hollow tube with a diameter of 10 mm inside a rectangular box imaged with an RCA 2-D array with a diverging lens ($f_{\#} = -1$) are shown in 40 dB dynamic range. The cyst box dimensions are 40×40×20mm^3. The C-planes are at a depth of 20 mm.

Diverging the wavefronts has the negative effect of lowering the pulse-echo energy as it is shown in Fig. 4 compared with the conventional row–column imaging using flat arrays. By using single element emissions with a fixed energy budget,

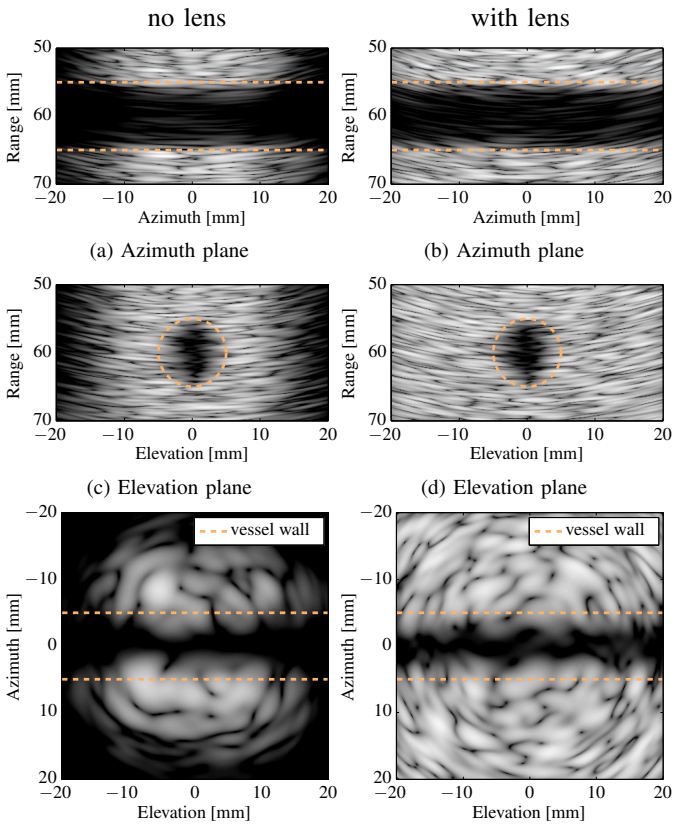

Figure 14. Three cross-planes (azimuth, elevation, and C-plane) of a hollow tube with a diameter of 10 mm inside a rectangular box imaged with an RCA 2-D array with a diverging lens ($f_{\#} = -1$) are shown in 40 dB dynamic range. The cyst box dimensions are $40\times40\times20\text{mm}^3$. The C-planes are at depth of 60 mm.

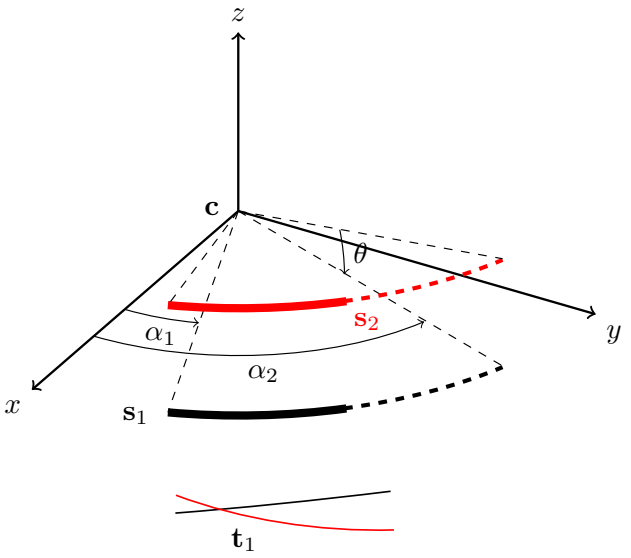

Figure 15. If each arc-shaped elements $\mathbf{s}_1$ and $\mathbf{s}_2$ is divided into two sub-elements, by activating each sub-element, only one intersection can be produced, $\mathbf{t}_1$ or $\mathbf{t}_2$ depending on which side has been activated. Thus, it is possible to accurately calculate the time-of-flight using only either row or column elements independently. Thereby, a two-way focusing profile can be achieved.

a certain volume region can be insonified, which is a trade-off between the penetration depth and the FOV. Thereby, the selection of the lens $f_{\#}$ depends on the specific application. For instance, in abdominal imaging, the flexibility that is provided by RCA arrays allows us to scale up the array aperture size, which corresponds to a higher generated pressure, a better contrast and spatial resolution, as well as a larger FOV. On the other hand, for applications, in which the imaging window is fixed, *e.g.*, cardiac imaging, the loss of the energy can be compensated for by using all the elements in transmit and placing the transmit focus in front of the array.

Using a diverging lens, the elements at the middle of the array can be represented as an arc, but the 3-D focusing characteristics of the off-center elements should make their representations more complicated. It requires to formulate the trigonometric functions that are used for delay calculations in a spherical geometry. It is also possible to have a different curvature in transmit and receive, however that requires to formulate the delay calculations in bispherical coordinates, which was beyond the scope of this study.

V. Conclusion

In this paper the quantitative imaging performance of a curved 62+62 RCA 2-D array was evaluated. The capabilities of a curved RCA 2-D array to effectively focus in both transmit and receive were investigated, and a suitable DAS beamformer introduced and implemented. Using SAI technique it was possible to image down to 14 cm at a volume rate of 88 Hz. The imaging performance with a curved RCA 2-D array at several different situations was evaluated based on simulations. Results confirm that using a diverging lens with $f_{\#} = -1$ can increase the imaging FOV to $60°\times60°$, and it is also possible to perform dynamic transmit-receive focusing throughout the curvilinear FOV. Thereby, the inherent imaging limitation with flat RCA 2-D arrays, *i.e.*, its forward looking rectilinear FOV, is overcome using a diverging lens. Overall, having a low channel count and a large FOV offers the potential to fabricate arrays with large aperture sizes, which is important for abdominal scans. Thus, by using a curved RCA 2-D array, 3-D imaging is possible with equipment in the price range of conventional 2-D imaging. These advantages might contribute to an increased use of real-time 3-D ultrasound imaging in medical diagnostics, and to the development of new clinical applications.

If each line-element can be divided into two equal sub-elements as shown in Fig. 15, by activating each sub-element of the row elements it is possible to eliminate either of those intersection points. The advantage of doing so is that, if the echoed signals are collected with the same transmitting elements, a two-way focusing profile can be produced, which is not possible with traditional row-column imaging since the transmit and receive apertures are perpendicular to each other. Therefore, by dividing the curvilinear FOV into 2 sub-volumes, each sub-volume can be beamformed with only row or column elements. Although this was not the main focus of this study, it could be interesting to investigate the focusing abilities using only the curved row or column elements.

ACKNOWLEDGMENT

This work was financially supported by grant 82-2014-4 from the Danish National Advanced Technology Foundation and from BK Ultrasound ApS, Herlev, Denmark.

REFERENCES

[1] C. E. Morton and G. R. Lockwood, "Theoretical assessment of a crossed electrode 2-D array for 3-D imaging," in *Proc. IEEE Ultrason. Symp.*, 2003, pp. 968–971.

[2] C. E. M. Démoré, A. Joyce, K. Wall, and G. Lockwood, "Real-time volume imaging using a crossed electrode array," *IEEE Trans. Ultrason., Ferroelec., Freq. Contr.*, vol. 56, no. 6, pp. 1252–1261, 2009.

[3] C. H. Seo and J. T. Yen, "A 256 x 256 2-D array transducer with row-column addressing for 3-D rectilinear imaging," *IEEE Trans. Ultrason., Ferroelec., Freq. Contr.*, vol. 56, no. 4, pp. 837–847, April 2009.

[4] A. Sampaleanu, P. Zhang, A. Kshirsagar, W. Moussa, and R. Zemp, "Top-orthogonal-to-bottom-electrode (TOBE) CMUT arrays for 3-D ultrasound imaging." *IEEE Trans. Ultrason., Ferroelec., Freq. Contr.*, vol. 61, no. 2, pp. 266–276, 2014.

[5] M. F. Rasmussen, T. L. Christiansen, E. V. Thomsen, and J. A. Jensen, "3-D imaging using row–column-addressed arrays with integrated apodization — Part I: Apodization design and line element beamforming," *IEEE Trans. Ultrason., Ferroelec., Freq. Contr.*, vol. 62, no. 5, pp. 947–958, 2015.

[6] R. K. W. Chee, A. Sampaleanu, D. Rishi, and R. J. Zemp, "Top orthogonal to bottom electrode (TOBE) 2-D CMUT arrays for 3-D photoacoustic imaging," *IEEE Trans. Ultrason., Ferroelec., Freq. Contr.*, vol. 61, no. 8, pp. 1393–1395, 2014.

[7] R. J. Zemp, W. Zheng, and P. Zhang, "Feasibility of top-orthogonal-to-bottom electrode (TOBE) 2D CMUT arrays for low-channel-count 3D imaging," in *Proc. IEEE Ultrason. Symp.*, 2011, pp. 498–502.

[8] Phillips, "http://www.healthcare.philips.com," February 2015.

[9] T. L. Christiansen, M. F. Rasmussen, J. P. Bagge, L. N. Moesner, J. A. Jensen, and E. V. Thomsen, "3-D imaging using row–column-addressed arrays with integrated apodization — part II: Transducer fabrication and experimental results," *IEEE Trans. Ultrason., Ferroelec., Freq. Contr.*, vol. 62, no. 5, pp. 959–971, 2015.

[10] A. W. Joyce and G. R. Lockwood, "Crossed-array transducer for real-time 3D imaging," in *Proc. IEEE Ultrason. Symp.*, 2014, pp. 2116–2120.

[11] H. Bouzari, M. Engholm, M. B. Stuart, S. I. Nikolov, E. V. Thomsen, and J. A. Jensen, "3-D imaging using row-column-addressed 2-D arrays with a diverging lens," in *Proc. IEEE Ultrason. Symp.*, 2016, pp. 1–4.

[12] J. A. Jensen and N. B. Svendsen, "Calculation of pressure fields from arbitrarily shaped, apodized, and excited ultrasound transducers," *IEEE Trans. Ultrason., Ferroelec., Freq. Contr.*, vol. 39, pp. 262–267, 1992.

[13] J. A. Jensen, "Field: A program for simulating ultrasound systems," *Med. Biol. Eng. Comp.*, vol. 10th Nordic-Baltic Conference on Biomedical Imaging, Vol. 4, Supplement 1, Part 1, pp. 351–353, 1996.

[14] B. Savord and R. Solomon, "Fully sampled matrix transducer for real time 3D ultrasonic imaging," in *Proc. IEEE Ultrason. Symp.*, vol. 1, 2003, pp. 945–953.

[15] C. Chang, K. Firouzi, K. K. Park, A. F. Sarioglu, A. Nikoozadeh, H. Yoon, S. Vaithilingam, T. Carver, and B. T. Khuri-Yakub, "Acoustic lens for capacitive micromachined ultrasonic transducers," *Journal of Micromechanics and Microengineering*, vol. 24, no. 8, p. 085007, 2014.

[16] J. A. Jensen, S. Nikolov, K. L. Gammelmark, and M. H. Pedersen, "Synthetic aperture ultrasound imaging," *Ultrasonics*, vol. 44, pp. e5–e15, 2006.

[17] D. Vilkomerson, J. Greenleaf, and V. Dutt, "Towards a Resolution Metric for Medical Ultrasound Imaging," in *Proc. IEEE Ultrason. Symp.*, 1995, pp. 1405–1410.

[18] K. Ranganathan and W. F. Walker, "Cystic resolution: A performance metric for ultrasound imaging systems," *IEEE Trans. Ultrason., Ferroelec., Freq. Contr.*, vol. 54, no. 4, pp. 782–792, 2007.

[19] D. A. Guenther and W. F. Walker, "Generalized cystic resolution: a metric for assessing the fundamental limits on beamformer performance," *IEEE Trans. Ultrason., Ferroelec., Freq. Contr.*, vol. 56, no. 1, pp. 77–90, January 2009.

Hamed Bouzari (S'14-M'16) received the B.Sc. degree from Mazandaran University, Iran, in 2006 and the M.Sc. degree from Zanjan University, Iran, in 2009, both in electrical engineering. He was a researcher at the Austrian Academy of Sciences (ÖAW), Vienna, Austria from 2010 to 2013. He received the Ph.D. degree in 2016 from the Technical University of Denmark, Kgs. Lyngby, Denmark, in biomedical engineering. He is currently a postdoctoral researcher with the Center for Fast Ultrasound Imaging (CFU) at the Technical University of Denmark. His research interests include all facets of high volume rate 3-D ultrasonic imaging for medical applications.

Mathias Engholm was born Copenhagen, Denmark, in 1989. He received his B.Sc. and M.Sc. degrees in engineering physics and nanotechnology from the Technical University of Denmark, Kgs. Lyngby, Denmark, in 2012 and 2015, respectively. He is currently pursuing a Ph.D. degree at the Technical University of Denmark, focusing on capacitve micromachined ultrasonic transducers for three-dimensional imaging.

Christopher Beers earned a M.S. degree in acoustics from The Pennsylvania State University in 2007, where his thesis research explored end-element anomalies in medical ultrasound transducer arrays. He has worked for Sound Technology, Inc. (Analogic/BK Ultrasound Group) since 2007, developing transducer technology and designing commercial medical ultrasound probes.

Matthias Bo Stuart (S'07-M'09) received the M.Sc. and Ph.D. degrees in Computer Engineering in 2006 and 2010 respectively, both from the Technical University of Denmark, Lyngby, Denmark. He is currently an Associate Professor in the Biomedical Engineering group at the Department of Electrical Engineering, Technical University of Denmark. His research interests include synthetic aperture methods for both anatomical and flow imaging in 2-D and 3-D, ultrasound systems, and real-time implementations of ultrasound processing algorithms.

Svetoslav Ivanov Nikolov (SM'11) received the M.Sc. degree in electrical engineering from the Technical University of Sofia, Sofia, Bulgaria, in 1996, and the Ph.D. degree from the Technical University of Denmark (DTU), Kongens Lyngby, Denmark, in 2001. He was an Associate Professor of Electronics and Signal Processing with DTU, from 2001 to 2009. In 2008, he joined BK Ultrasound, Herlev, Denmark, to work on the commercial implementation of the technologies developed at DTU.

Dr. Nikolov has been an Analogic Fellow since 2015 as recognition for his work in research and development.

Erik Vilain Thomsen was born in Aarhus, Denmark, in 1964. He received the M.Sc. degree in physics from the University of Southern Denmark, Odense, Denmark, and the Ph.D. degree in electrical engineering from the Technical University of Denmark (DTU), Kongens Lyngby, Denmark, in 1998. He is currently a Professor with DTU Nanotech, DTU, where he is also the Head of the MEMS Applied Sensors Group. He teaches classes in solid-state electronics, microtechnology, and nano and microfabrication. His current research interests include capacitive micromachined ultrasonic transducers, MEMS multisensors, biomedical devices, energy harvesting devices, and piezoelectric MEMS.

Dr. Thomsen received the AEG Electron Prize in 1995, and has received several teaching awards at DTU.

Jørgen Arendt Jensen (M'93-SM'02-F'12) received the Master of Science degree in electrical engineering in 1985 and the Ph.D. degree in 1989, both from the Technical University of Denmark. He received the Dr.Techn. degree from the university in 1996.

Since 1993, he has been Full Professor of Biomedical Signal Processing with the Department of Electrical Engineering, Technical University of Denmark and head of the Center for Fast Ultrasound Imaging since its inauguration in 1998. He has published more than 450 journal and conference papers on signal processing and medical ultrasound and the book Estimation of Blood Velocities Using Ultrasound (Cambridge Univ. Press), 1996. He is also the developer and maintainer of the Field II simulation program. He has been a visiting scientist at Duke University, Stanford University, and the University of Illinois at Urbana-Champaign. He was head of the Biomedical Engineering group from 2007 to 2010. In 2003, he was one of the founders of the biomedical engineering program in Medicine and Technology, which is a joint degree program between the Technical University of Denmark and the Faculty of Health and Medical Sciences at the University of Copenhagen. The degree is one of the most sought-after engineering degrees in Denmark. He was chairman of the study board from 2003 to 2010 and Adjunct Professor with the University of Copenhagen from 2005 to 2010. He has given a number of short courses on simulation, synthetic aperture imaging, and flow estimation at international scientific conferences and teaches biomedical signal processing and medical imaging at the Technical University of Denmark. His research is centered around simulation of ultrasound imaging, synthetic aperture imaging, vector blood flow estimation, and construction of ultrasound research systems.

Dr. Jensen has given more than 60 invited talks at international meetings and received several awards for his research.